

RSC Advances



This is an *Accepted Manuscript*, which has been through the Royal Society of Chemistry peer review process and has been accepted for publication.

Accepted Manuscripts are published online shortly after acceptance, before technical editing, formatting and proof reading. Using this free service, authors can make their results available to the community, in citable form, before we publish the edited article. This *Accepted Manuscript* will be replaced by the edited, formatted and paginated article as soon as this is available.

You can find more information about *Accepted Manuscripts* in the [Information for Authors](#).

Please note that technical editing may introduce minor changes to the text and/or graphics, which may alter content. The journal's standard [Terms & Conditions](#) and the [Ethical guidelines](#) still apply. In no event shall the Royal Society of Chemistry be held responsible for any errors or omissions in this *Accepted Manuscript* or any consequences arising from the use of any information it contains.

Integrated electrospun carbon nanofibers with vanadium and single-walled carbon nanotubes through covalent bond for high-performance supercapacitor

84Cite this: DOI: 10.1039/x0xx00000x

Received 00th January 2012,
Accepted 00th January 2012

DOI: 10.1039/x0xx00000x

www.rsc.org/

Kexin Tang^{abc}, Yuping Li^{*b}, Hongbin Cao^{abc}, Feng Duan^b, Jason Zhang^a,
Yi Zhang^{abc}, Yi Wang^b

We report a ternary composite vanadium/single-walled carbon nanotubes (SWCNTs)/carbon nanofibers (VSCNFs) materials using hybrid-electrospinning and carbonizing of polyacrylonitrile, polyvinylpyrrolidone, SWCNTs and vanadyl acetylacetonate. The morphology and structure of the ternary composites are characterized. Its electrochemical properties are measured in 6 mol L⁻¹ aqueous KOH electrolyte. VSCNFs possesses hierarchical structure with micropores and mesopores and specific surface area of 821 m² g⁻¹, and it also exhibits reversible specific capacitance of 479 F g⁻¹ at 1 A g⁻¹ and 367.4 F g⁻¹ at 10 A g⁻¹, and remains 94% of initial capacitance after 5000 cycles (8 A g⁻¹). The results show that simultaneously adding vanadium and SWCNTs can greatly enhance the conductivity, capacitive performance and stability by forming closer connection with nanofibers through V-N-C, V-O-C and V=O bonds. SWCNTs are not only mechanically mixed in CNFs to enhance the extent of graphitization, but also involved in the transmutation process of CNFs graphitization with participation of vanadium.

1. Introduction

To meet the increasing demands for clean and sustainable energy, high-capacity energy storage devices like supercapacitor have attracted more attention¹. According to the charge storage mechanisms, three types of supercapacitors are summarized²: electronic double layer (EDL) capacitor, pseudo-capacitor and hybrid capacitor. EDL capacitor usually possesses short charge time, long cycling life and high power density, but its storage capabilities need to be improved. In comparison, pseudo-capacitor has higher current response due to the chemical reactions on the interface of electrode, while the disappointing capacitance retention limits its further application. Consequently, hybrid capacitor, that combines both the advantages of EDL capacitor and pseudo-capacitor, has been developed for getting extraordinary performance.

Due to the abundant storage, low cost and relative high structure stability, carbon materials are most commonly used in supercapacitors^{3, 4}, such as activated carbon⁵, carbon nanofibers⁶, carbon aerogels⁷, ordered mesoporous carbon⁸, carbon nanotubes⁹, carbon black¹⁰ and graphene¹¹, especially two or more carbon materials are composited together to achieve sophisticated structure and characteristics^{4, 12, 13}, like three-dimensional network¹⁴, where activated carbon (AC), graphene or carbon nanofibers (CNFs) usually acts as carbon skeleton, and carbon nanotubes (CNTs) or carbon black (CB) acts as ancillary elements. For example, single-walled carbon nanotubes (SWCNTs) are sometimes used as additive for CNFs electrode because of its high conductivity and large effective

specific surface area¹⁵, and it also can help to build hierarchical pore structure¹⁶.

Metal oxides such as TiO₂, RuO₂, MnO₂, and VO_x, are widely used to modify carbon materials to get pseudo-capacitance^{17, 18}. RuO₂ is reported to be one of the most effective additives, but its high price limited its application^{5, 19}. TiO₂ composite carbon nanofibers are more likely used in photocatalysis research^{20, 21}. One of the most development MnO₂ modified carbon electrode show relative low capacitance²². V₂O₅ (vanadium pentoxide)²³⁻²⁵, VO₂ (vanadium dioxide)^{26, 27} and organic vanadium²⁸ are reported to modify porous carbon electrode, while the insulation of these compound weaken carbon nanofibers conductivity and pore structure, but still vanadium compounds might be a suitable additives due to its relatively low cost and abundance in China²⁹. There are two distinctive formations of vanadium compound inserted in the carbon electrode, namely, amorphous vanadium and crystal vanadium oxide. Some studies show that amorphous vanadium may exhibit more superior capacitive properties compared to crystal vanadium^{27, 28, 30}, because amorphous vanadium is likely linked to carbon skeleton with covalent bonds in atom level, and thus enhance the contact of transition metal with ions. In comparison, the crystal vanadium is physically dispersed in the carbon skeleton. Thus, the research on single-step synthesis and simultaneously incorporating vanadium and conductive additives to form an integrated structure with tunable pore distribution and efficient surface area and good conductivity may be a possible approach to achieve high performance and steady supercapacitor.

Electrospinning technique is a simple and versatile method for producing continuous nanofibers from polymers, composites or ceramics³¹. In this work, we have successfully synthesized a composite vanadium/SWCNTs/CNFs electrode for supercapacitors with hybrid electrospinning and carbonization techniques. The fabricated composite CNFs (VSCNFs) have achieved advantages as follows: (1) hierarchical structure, which can enhance ion diffusion within CNFs; (2) unique V-N-C bond to combine carbon skeleton and graphite fragments; (3) high extent of graphitization to improve structure regularity and conductivity; (4) high capacitance, and stable electrochemical cyclic properties. This work provides a performable method of synthesizing stably composited metal-carbon materials and predicts the vanadium and SWCNTs involved structure.

2. Experimental

2.1. Materials preparation

Polyacrylonitrile (PAN, $M_w = 150,000$) was purchased from Sigma-Aldrich (USA). Polyvinylpyrrolidone (PVP, $M_w = 1,300,000$) was obtained from Aladdin (China). Vanadyl (IV) acetylacetonate ($\text{VO}(\text{acc})_2$, purity > 98%) was bought from J&K (China). All other chemicals used in this work were purchased from Beijing Chemical Industry Group (China). Single-walled carbon nanotubes (SWCNTs, purity > 95%, OD < 2nm) were purchased from Shenzhen Nanotech Port (China). SWCNTs were simply treated with diluted nitric acid to remove little residential metal catalyst.

Preparation of electrospun precursor. The CNFs webs were synthesized by electrospinning method followed with pre-oxidizing and carbonizing process. Electrospinning solutions were prepared by the following steps: a certain amount of SWCNTs was dispersed in 30 mL dimethyl formamide (DMF) with ultrasonic for 2 h to obtain uniform suspension, and then 2.845 g PAN and 2.845 g PVP were blended into the obtained SWCNTs/DMF suspension by stirring, after that, $\text{VO}(\text{acc})_2$ was added into the mixtures. Finally the mixtures were stirred at 60 °C for 12 h to obtain a homogenous and stable suspension. Accordingly, six kinds of electrospinning solutions were prepared by varying the amount of SWCNTs and $\text{VO}(\text{acc})_2$ (Table 1).

Electrospinning process. The homogeneous electrospinning solutions were loaded into a 30 mL syringe connected with an 18G needle as a spinneret. The electrospinning was performed on a TL-01 electrospinning machine (Nabont, China) under the conditions described as follows: a flow rate of 1 mL h^{-1} , a tip-to-collector distance of 15 cm, the spinneret reciprocating horizontal speed of 10 cm min^{-1} , and the collector covered with aluminium foil rotating at 500 rpm. A high voltage of 12 KV

was applied to the spinneret. Especially, a negative voltage of -5 KV was applied to collector to obtain more uniform diameters and dense mat. The temperature was maintained at 35 °C.

Pre-oxidation and carbonization processes. Composited nanofibers webs were oxidized and carbonized in a tube furnace. According to literatures^{32, 33}, a transitional oxidizing procedure is more suitable to avoid the skin-core structure and form uniform intensity and continuous fibres for the oxidized nanofibers compared to a constant oxidizing temperature of 280 °C. Pre-oxidation process was conducted with air flow rate of 200 mL min^{-1} for certain time, and then, the samples were carbonized at 800 °C or 900 °C, with N_2 flow rate of 400 mL min^{-1} . The conditions of pre-oxidization and carbonization are summarized in Table S1 of Supplementary Materials. Finally, the dominations of differential conditions and content of nanofibers are summarized in Table 1.

2.2 Morphology and structure characterization

The morphology and element contents of samples were observed by a field emission scanning electron microscopy (FE-SEM, JSM-7001F, JEOL, Japan) equipped with energy dispersive spectrometer (EDS, INCA X-MAX, Oxford Instruments, UK). Thermal gravity analysis and differential scanning calorimetry was performed in a TGA/DSC1 STARE System (Metler Toledo, Switzerland). High resolution field emission transmission electron microscopy (TEM, JEM 2100F, JEOL, Japan) was employed to observe samples inner structure. X-ray diffraction (XRD) was conducted on SmartLab (Rigaku, Japan). Raman spectroscopy was obtained on LabRAM HR800 (Horiba Jobin Yvon, French). Fourier transform infrared spectroscopy (FT-IR) was obtained on a Spectra spectrometer (Nicolet iS50, Thermo Fisher Scientific, USA). X-ray photoelectron spectroscopy (XPS) was measured using ESCALAB 250Xi spectrometer (Thermo Fisher Scientific, United States). Nitrogen sorption isotherm curves of samples were obtained by automatic specific surface analyzer (Quantachrome, United States) at liquid nitrogen boiling point of 77 K, and the samples were outgassed at 200 °C for 8 h before measurement. Brunauer-Emmett-Teller (BET) method was used to calculate the specific surface area (S_{BET}). Pore size distribution (PSD) and total pore volume was calculated by the density function theory (DFT), and the volume of micropores was provided by Horvath-Kawazoe (HK) method.

2.3 Electrochemical measurements

Samples electrochemical performances were studied in a typical three-electrode system on Autolab electrochemical workstation (PGSTAT302N, Metrohm, Switzerland). The working electrode (WE) was fabricated by pressing

Table 1 Preparation conditions and denominations of nanofibers.

Samples	Pure PAN/PVP	SWCNTs +PAN/PVP	$\text{VO}(\text{acc})_2$ +PAN/PVP	$\text{VO}(\text{acc})_2$ +SWCNTs +PAN/PVP		
				10% $\text{VO}(\text{acc})_2$	15% $\text{VO}(\text{acc})_2$	20% $\text{VO}(\text{acc})_2$
Precursor nanofibers	PNFs	SNFs	VNFs	10VSNFs	15VSNFs	20VSNFs
Carbonized at 800 °C	PCNFs-800	SCNFs-800	VCNFs-800	10VSCNFs-800	15VSCNFs-800	20VSCNFs-800
Carbonized at 900 °C	PCNFs-900	SCNFs-900	VCNFs-900	10VSCNFs-900	15VSCNFs-900	20VSCNFs-900

activated materials and nickel foams under a pressure of 10 MPa for 1 min, where the as-synthesized materials act as active composite and nickel foams act as current collector, and the size of WE was 1 cm × 1 cm × 260 μm (contains two layers of pressed nickel foams and one layer of activated materials), and the average mass for activated materials is about 3 mg. The reference electrode was Hg/HgO electrode immersed in 1M potassium hydroxide aqueous solution (KOH). The counter electrode (CE) was platinum sheet with an area of 1 cm². The electrolyte was 6M KOH. Cyclic voltammetry (CV) measurements were performed in a voltage window from -1.0 to 0 V (vs. Hg/HgO) at scan rates of 5, 10, 20, 30, 40, 50, 80 to 100 mV s⁻¹. Galvanostatic charge-discharge (GCD) tests were conducted at current densities of 1, 2, 5, and 10 A g⁻¹ based on active materials weight of WE. Electrochemical impedance spectroscopy (EIS) information was obtained in range of 10⁵ Hz ~ 0.01 Hz at open circuit potentials with an amplitude signal model of 5 mV.

The specific capacitance (F g⁻¹) obtained from CV method is based on equation (1):

$$C_{\text{GCD}} = \frac{\int_V^{V+\Delta V} I \times dV}{2 \times s \times \Delta V \times m} \quad (1)$$

Where I (A) is the current response at potential of dV , s (mV s⁻¹) is the scan rate, ΔV (V) is the potential window, m (g) is the activated materials mass.

The specific capacitance (F g⁻¹) derived from GCD curves (mean value over discharging time) is calculated from the equation (2):

$$C_{\text{GCD}} = \frac{I(t) \times \Delta t}{\int_0^t (dV(t)/dt) dt \times m} \quad (2)$$

Where Δt (s) is the corresponding discharging time, $I(t)$ (A) is the discharging current at time 't', $V(t)$ (V) is the discharging potential at time 't', m (g) is the weight of active material.

3. Results and discussion

3.1 Morphology and structure

Uniform diameter distribution and continuous nanofibers of precursor and carbonized samples are observed from Fig. S1 (supplementary information), indicating stable electrospinning and carbonizing process. The FE-SEM images show the smooth surface of PNFs and SNFs without apparent black spot or agglomeration (Fig. 1-a1, b1), indicating that the activation and oxidation of SWCNTs are helpful for regular distribution in the nanofibers. Contrastively, VNFs and VSNFs present rougher surface, and the surface become smooth after carbonization (Fig. 1-c, d). The average diameter of SNFs (540 nm) is smaller than others (Table S2), suggesting additives conductivity influences precursor nanofibers diameter, because the

conductivity of SWCNTs is better than the organic compound VO(acc)₂³⁴⁻³⁷. After pre-oxidation and carbonization, CNFs are dramatically shrunk and overlapped. Notably, the CNFs overlapping would greatly enhance the conductivity of CNFs webs. Table 2 presents the elementary composition of composite nanofibers. The carbon ratio of the samples is increased after adding SWCNTs and decreased after loading VO(acc)₂, and 15VSCNFs-800 has nearly the same nitrogen and oxygen content with VCNFs-800, only except substituting amount of 4 wt.% vanadium for carbon. Carbonization degree is enhanced by increasing annealed temperature. However, the excessive cyclization and cross-linking reactions of polymers in higher temperature may cause surface defects (Fig. 1d3). The vanadium load in 15VSCNFs-800 is 8 %, and its atom ratio of carbon, oxygen, nitrogen and vanadium is 39:5:3:1. Notably, nitrogen element content is significantly decreased after carbonization, but it's still a significant content that can influence electrode performance^{25, 38} due to the surplus electron pair of nitrogen. Consequently, uniform composite CNFs webs have been obtained through electrospinning and carbonization, and SWCNTs and vanadium have been successfully inserted into nanofibers.

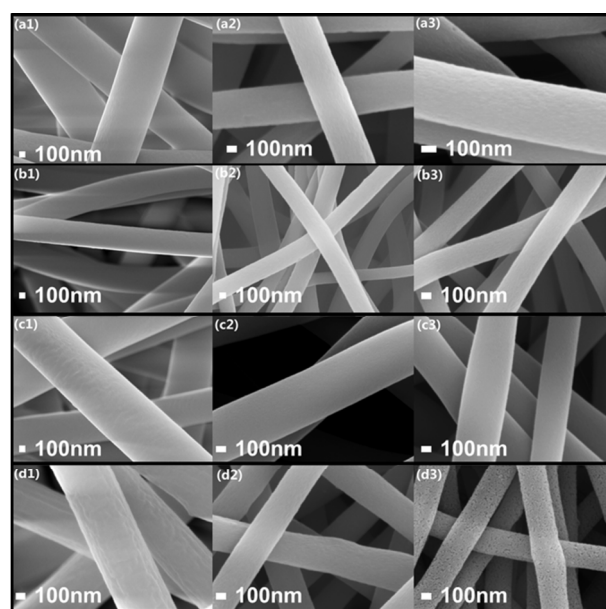


Fig. 1 Field emission scanning electron microscopy images of nanofibers: (a1-a3) PNFs; PCNFs-800 and PCNFs-900; (b1-b3) SNFs, SCNFs-800 and SCNFs-900; (c1-c3) VNFs, VCNFs-800 and VCNFs-900; (d) 15VSNFs, 15VSCNFs-800 and 15VSCNFs-900.

Table 2 The weight ratio of C, N, O and V atom in precursor nanofibers and carbon nanofibers.

Atom	PNFs	PCNFs		SNFs	SCNFs		VNFs	VCNFs		15VSNFs	15VSCNFs	
		800	900		800	900		800	900		800	900
C	67.7	81.8	86.8	67.0	85.0	90.2	69.2	78.0	81.6	67.0	74.0	82.5
N	22.5	12.1	5.8	22.9	7.4	3.6	18.1	6.5	4.2	19.9	6.3	4.8
O	9.8	6.1	7.4	10.1	7.6	6.2	11.6	10.2	8.8	11.4	11.7	4.2
V	0	0	0	0	0	0	1.1	5.3	5.4	1.7	8.0	8.5

Table 3 Pore structure and properties of PCNFs, SCNFs, VCNFs, and VSCNFs

Samples	PCNFs		SCNFs		VCNFs		10VSCNFs		15VSCNFs		20VSCNFs	
	800	900	800	900	800	900	800	900	800	900	800	900
S_{BET} ($\text{m}^2 \text{g}^{-1}$)	642	683	696	730	721	106	817	343	821	168	418	101
V_{mic} ($\text{cm}^3 \text{g}^{-1}$)	0.292	0.302	0.280	0.292	0.184	0.052	0.285	0.082	0.310	0.063	0.178	0.041
V_{total} ($\text{cm}^3 \text{g}^{-1}$)	0.321	0.327	0.370	0.388	0.308	0.194	0.395	0.269	0.470	0.218	0.327	0.183
$V_{\text{mic}}/V_{\text{total}}$ (%)	91.0%	92.4%	75.7%	75.3%	59.7%	26.8%	72.2%	30.5%	66.0%	28.9%	54.4%	22.4%

*1. S_{BET} is abbreviation of the specific surface area calculated from Brunauer-Emmett-Teller (BET) method, and V_{mic} and V_{total} are the effective adsorption volume of micropores and total volume.

Fig. 2 displays the N_2 sorption isotherm curves of as-synthesized samples. PCNFs electrode exhibits typical type-I Langmuir adsorption behaviour (**Fig. 2a**) according to IUPAC, and other five samples carbonized at 800 °C possess hierarchical structure with micropores and mesopores (**Fig. 2b**), which can be distinguished through the small adsorption hysteresis during pressure P/P_0 from 0.8 to 0.3 as well as the strong adsorption behaviour during low pressure ($P/P_0 < 0.1$). As shown in **Table 3**, SCNFs ($696 \text{ m}^2 \text{g}^{-1}$) have slightly larger specific surface area (S_{BET}) compared to PCNFs ($642 \text{ m}^2 \text{g}^{-1}$), and the S_{BET} of VCNFs is slightly increased after inserting vanadium, but the micropores volume ratio is decreased, which impairs electrochemical performance², and adding vanadium and SWCNTs into PCNFs can hold S_{BET} and micropores volume ratio simultaneously. This can be explained as follows: according to references^{28, 32, 39}, carbonization process of composite PAN/PVP nanofibers contains two pathways: I. Polymer cross-linking and pyrolysis; II. Competitive reactions between $\text{VO}(\text{acc})_2$ and polymer skeleton. Carbonization process of PNFs and SNFs without $\text{VO}(\text{acc})_2$ is driven by pathway I, resulting almost pure micropores, meanwhile, VNFs and VSNFs are driven by both pathway I and II, resulting expanded mesopores. On the other hand, the opened SWCNTs with inner diameter less than 2 nm can increase the ratio of micropores and the specific surface area, and the external structure of SWCNTs may also facilitate the generation of mesopores to enlarge the ion channel. However, excessive $\text{VO}(\text{acc})_2$ (20 wt. %) overly strengthen pathway II, resulting serious S_{BET} and micropores volume ratio decline.

Carbonizing temperature could affect the pore structure of CNFs as well. When raising carbonizing temperature from 800 °C to 900 °C, the S_{BET} of PCNFs and SCNFs increase from 642, 696 to 683, 730 $\text{m}^2 \text{g}^{-1}$, respectively. However, the S_{BET} of VCNFs, VSCNFs decrease dramatically. This may due to the enhanced reaction of pathway II when raising temperature. These results indicate that raising carbonized temperature is a feasible method to enhance structure property of vanadium-free carbon materials, but to vanadium-composited sample, carbonized temperature varying method is undesirable.

The transmission electron microscopy (TEM) images show the morphology and surface pore structure of PCNFs-800, SCNFs-800 and 15VSCNFs-800 (**Fig. 3, Fig. S9**). PCNFs-800 and SCNFs-800 present denser structure than 15VSCNFs-800 although they have similar diameter around 350 nm. The reason is that 15VSCNFs-800 possesses larger ratio of mesopores than PCNFs and SCNFs (**Fig. 2b**), and it is supposed that the mesopores in 15VSCNFs-800 lead some electron beams generated by laser in TEM to penetrate the edge of CNFs and finally to present looser internal structure. The core of CNFs shows black possibly because those mesopores are arranged irregular and vermicular^{40, 41} (**Fig. 3d, Fig. S9d**).

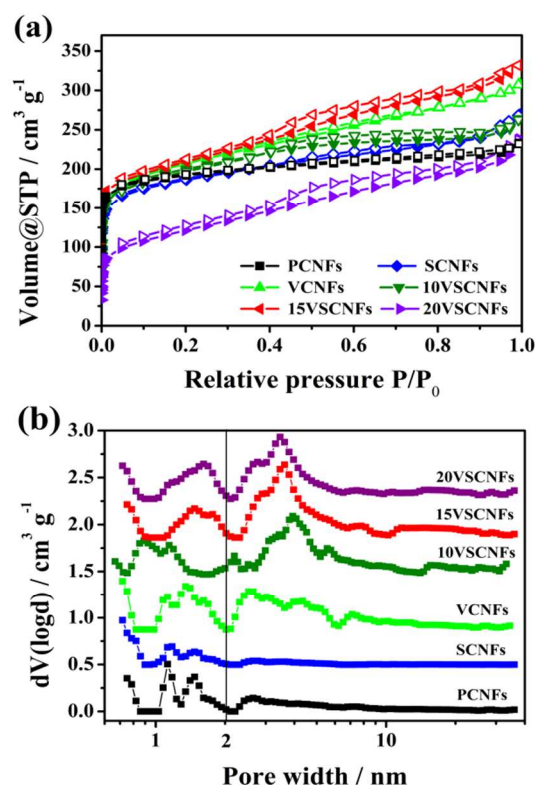


Fig. 2 Nitrogen isothermal adsorption analysis: (a) Nitrogen adsorption isotherm curves and (b) pore size distribution plots of samples carbonized at 800 °C.

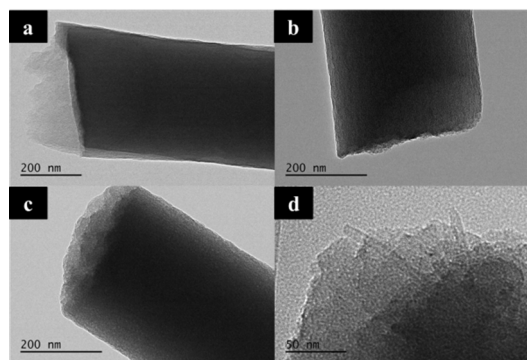


Fig. 3 Transmission electron microscopy images: (a) PCNFs-800, (b) SCNFs-800, (c) 15VSCNFs-800 and (d) high magnification image of 15VSCNFs-800

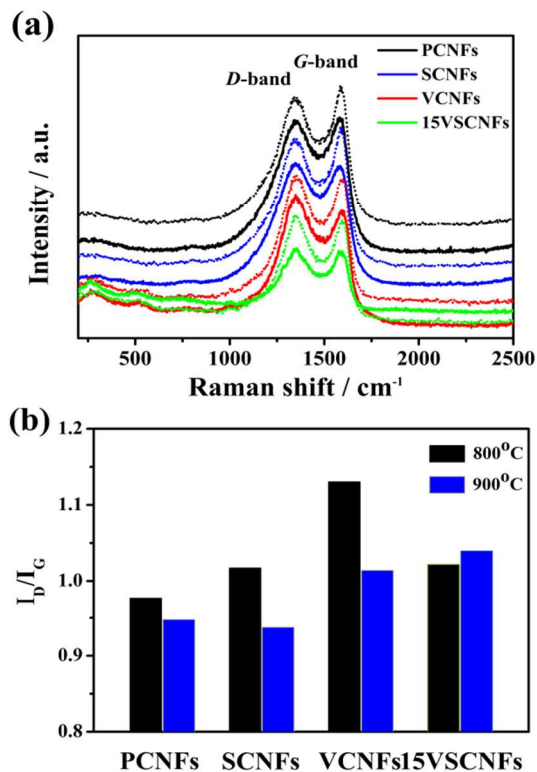


Fig. 4 Analysis of carbon defects of samples: (a) Raman spectra and (b) the ratio of I_D and I_G (I_D / I_G) of PCNFs, SCNFs, VCNFs and 15VSCNFs. (The solid line and short dot line for (a) represent samples carbonized at 800 °C or 900 °C, respectively).

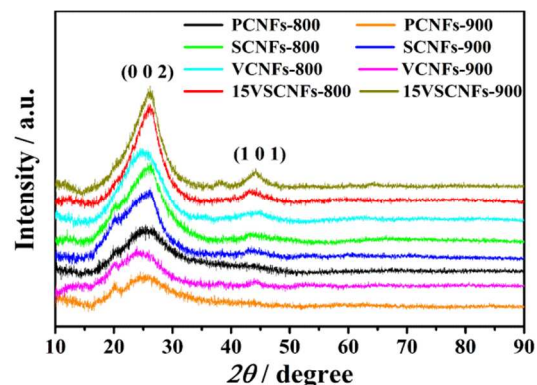


Fig. 5 X-ray diffraction curves of PNFs, SCNFs, VCNFs, and 15VSCNFs carbonized at 800 °C or 900 °C. The (0 0 2) peak and (1 0 1) peak represents graphitic structure and turbostratic carbon structure, respectively.

Table 4 Binding energy values (eV) from XPS spectrum and reference of V2p, N1s, and O1s.

Element	N1s	O1s	V2p _{3/2}	V2p _{1/2}
 Ferrer ⁴²	399.1	532.9	516.5	524.3
 This work	398.9	532.9	516.4	524.4

Fig. 4 shows the Raman spectroscopy of the composited CNFs. Two peaks at 1360 cm^{-1} and 1580 cm^{-1} are obtained (**Fig. 4a**), corresponding to the *D*-band for amorphous carbon and *G*-band for orderly graphitized carbon, respectively^{43,44}. The ratio of relative intensity of *D*-band and *G*-band (I_D / I_G), which represents the extent of carbon defects, is summarized in Fig. 4b. For SWCNT-free CNFs, the I_D / I_G value of VCNFs-800 is much higher than that of PCNFs. On the contrary, no obvious increase of I_D / I_G is observed after embedding SWCNTs. I_D / I_G of samples at 900 °C is smaller than that at 800 °C except for 15VSCNFs (**Fig. 4b**), suggesting that the graphitic sheets should be continuously growing when carbonized temperature is increased, and for 15VSCNFs, the exothermic reactions between VO(acc)₂ and PAN/PVP may be accelerated when carbonized temperature and VO(acc)₂ content were increased simultaneously. Therefore, adding 15% VO(acc)₂ and 10% SWCNTs within electrospun precursors is a highly effective approach to improve the graphitizing extent of composite CNFs.

The effects of SWCNTs content, VO(acc)₂ content and carbonizing temperature on crystal structure of CNFs are studied by XRD (**Fig. 5**). Two diffractive peaks are observed at $2\theta \approx 25^\circ$ and 43° , which are attributed to graphitic structure (0 0 2) and turbostratic carbon structure (1 0 1), respectively⁴⁴. It's obvious that the (0 0 2) peak gets sharper and gradually shifts right ($2\theta \approx 26^\circ$) when SWCNTs are added into CNFs, confirming that SWCNTs have been successfully loaded. The (0 0 2) peak of CNFs also turns sharper and stronger after loading vanadium; this can be explained that vanadium may participate graphitizing process and enhance the extent of graphitization. Furthermore, vanadium in CNFs may be amorphous as vanadium oxide peaks are failed to be detected³⁰. The (0 0 2) peak and (1 0 1) peak are both slightly magnified when carbonizing temperature is increased from 800 °C to 900 °C, confirming the graphitization and turbostratic structure are both enhanced. The Raman and XRD results show that SWCNTs are not only mechanically mixed in CNFs to enhance the extent of graphitization, but also involved in the transmutation process of CNFs graphitization with the participation of VO(acc)₂.

3.2 Integrated structure with vanadium and SWCNTs involved

The morphological and structure characterizations suggest that there is an integrated structure formed between vanadium and carbon skeleton with participating of SWCNTs. For clearly understanding of the structure and chemical bond between vanadium and carbon skeleton, XPS spectrum of 15VSCNFs-800 was obtained (**Fig. 6**). The peaks of carbon (C1s), oxygen (O1s), nitrogen (N1s) and vanadium (V2p) are observed at the survey region (**Fig. 6a**). The C1s spectrum shows four peaks at 284.7 eV, 285.4 eV, 286.7 eV and 289.7 eV, corresponding to C-C, C-N, C-O, and C=O bonds⁴⁵, respectively (**Fig. 6b**). Nitrogen may exist in four types, which are N-V (398.9 eV), R-N (401.5 eV), C≡N and EWGs-N (electron withdrawing groups) (402.2 eV)⁴⁶ (**Fig. 6c**). For the vanadium element, it could link to carbon skeleton through V-O-C and V=O bonds²⁸. However, V-N-C bond may also exist in CNFs. The binding energy of V2p_{3/2}, N1s, and C1s is consistent with literature⁴² (**Fig. 6e**), and **Table 4** illustrates the corresponding binding energy; this structure could strengthen CNFs by offsetting the defects caused by the pyrolysis of PAN/PVP and VO(acc)₂. Notably, the V-C bond is unlikely to exist as no peaks are observed at 282.5 eV for C1s and 513.5 eV for V2p_{3/2}⁴⁷.

TGA/DSC method has been conducted to promote the understanding of the thermal behaviours after inserting

vanadium and SWCNTs. As shown in **Fig. 7**, the sharp exothermic peaks around 300 °C are observed obviously, mainly due to the cyclization and oxidation reaction of PAN and PVP³², and the small endothermic peak around 480 °C is caused by dehydrogenation and excessive oxidation of PAN, and the wide exothermic peak from 500 °C to 800 °C is about the further dehydrogenation and intensively cyclization of carbon skeleton³². The decomposition of PVP mainly happens at 600 °C³⁹. With the increase of vanadium content, the weight loss rate slows down, and SWCNTs barely influence the weight loss (**Fig. 7a**). The embedded vanadium could influence carbonizing process in two competitive ways: firstly, VO(acc)₂ would be connected to carbon skeleton during the pyrolysis process of PAN and PVP, which may produce micropores and mesopores with emitting of N₂, CO, CO₂, HCN, etc.³², resulting in accelerating the pyrolysis process (**Fig. 7b**) and more serious weight loss. Secondly, the replacement of C, N, H atoms with vanadium atom which has higher relative molecular weight would greatly slow down the weight loss. **Fig. 7c** displays the Raman spectra of 15VSCNFs-800. Four distinguishable variations are observed for the following Raman peaks: 1010 [$\nu(\text{V}=\text{O})$], 749 [$\nu_{as}(\text{V}-\text{O})$], 501 [$\nu_s(\text{V}-\text{O})$], and 267 cm⁻¹ [$\nu(\text{V}-\text{N})$], which are in accordance with references^{48, 49}. Combining with analysis from XPS, this provides the direct information about the new formed V-O-C, V-N-C and V=O bonds.

Based on above discussion, we predict the vanadium-involved graphite skeleton structure (**Fig. 7d**). According to the atom ratio of 15VSCNFs-800, there are three kinds of possible structure: V-O-C and V-N-C can link graphene fragments into large graphite sheets, or V⁴⁺ substitute for carbon atom, or V³⁺ bond with carbon skeleton margin through (O=)V-O-C form to cause faradic response when applying for capacitive devices. Notably, V-O-C and V-N-C covalent bonds may not only exist between fragments, but also bond between two layers to form multiple layers graphite. This structure can store more electrons when charging the electrode. However, due to the molecular structure of carbon, nitrogen and vanadium, the desultory carbon skeleton would wave naturally; consequently this structure would form much steric hindrance for storing electrons and lead to increase of carbon disorder and amorphous, so SWCNTs (OD < 2nm) can support between carbon skeleton to separate layer, prompt graphite flake growth and act as conductive tunnel.

3.3 Electrochemical performance

Cyclic voltammetry (CV) method is a direct way to characterize electrodes capacitive ability. **Fig. 8** describes CV curves of PCNFs-800, SCNFs-800, VCNFs-800 and 15VSCNFs-800. The CV shape of SCNFs-800 is closer to rectangle than that of PCNFs-800 (**Fig. 8-a,b**), and the as-calculated C_{CV} of SCNFs-800 is improved with increasing scan rates, however, C_{CV} rate performance of PCNFs-800 is reduced, indicating that the former is closer to the ideal double layer supercapacitor behaviour⁴⁴. The CV curves of VCNFs-800 and 15VSCNFs-800 are deformed seriously as compared to PCNFs-800 (**Fig. 8-c,d**), indicating that adding vanadium without SWCNTs reduces the stability of electrode when increasing scan rates, but SWCNTs can make up capacitive performance by enhancing current response due to the developed porous integrated structure.

The two peaks of VCNFs-800 and 15VSCNFs-800 at reduction potential of -0.9 V and oxidation potential of -0.3 V are possibly corresponding to the redox of vanadium-related groups in composite CNFs²⁸, suggesting pseudo-capacitive behaviour (**Fig. 8e**). The CV area at 5 mV s⁻¹ is increased from PCNFs, SCNFs, VCNFs to 15VSCNFs, suggesting both SWCNTs and vanadium can enhance PCNFs capacitive performance, but in different ways: the former enhance conductivity, and the latter introduce pseudo-capacitance. As predicted previously, the integrated 15VSCNFs combine these

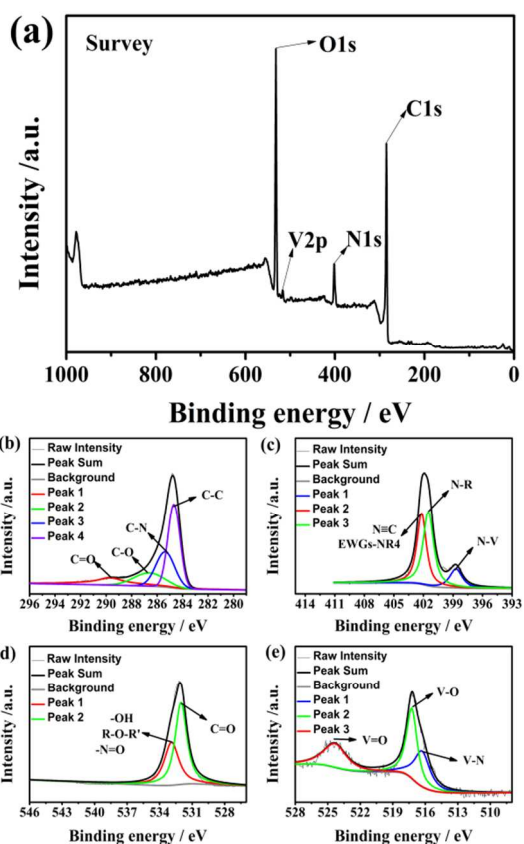


Fig. 6 X-ray photoelectron spectroscopy of 15VSCNFs-800: (a) survey scan, and peak curves of (b) C1s, (c) N1s, (d) O1s, and (e) V2p.

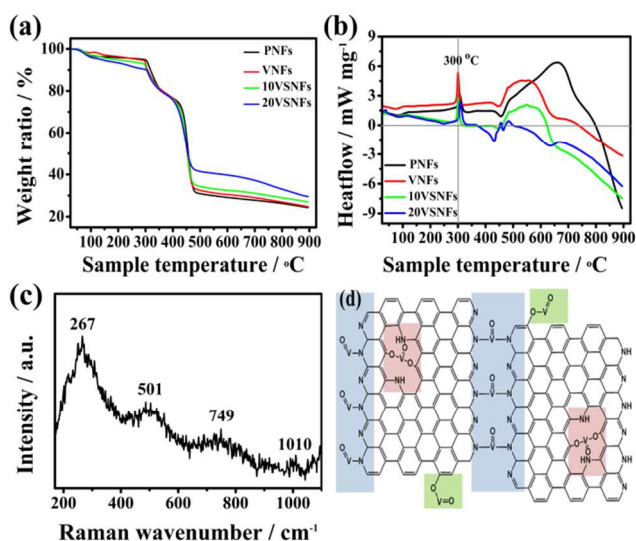


Fig. 7 Thermal behaviour analysis of electrospun precursors: (a) Thermal gravity analysis and (b) Differential scanning calorimetry curve of precursor nanofibers: PNFs, VNFs, 10VSNFs and 20VSNFs with N₂ following at 60 mL min⁻¹ with heating rate of 10 °C min⁻¹. (c) Raman spectra of 15VSCNFs-800 with wavenumber from 1100 to 150 cm⁻¹. (d) Predicted integrated graphite structure of V-N-C and V-O-C, and V=O bonds involved in carbon skeleton.

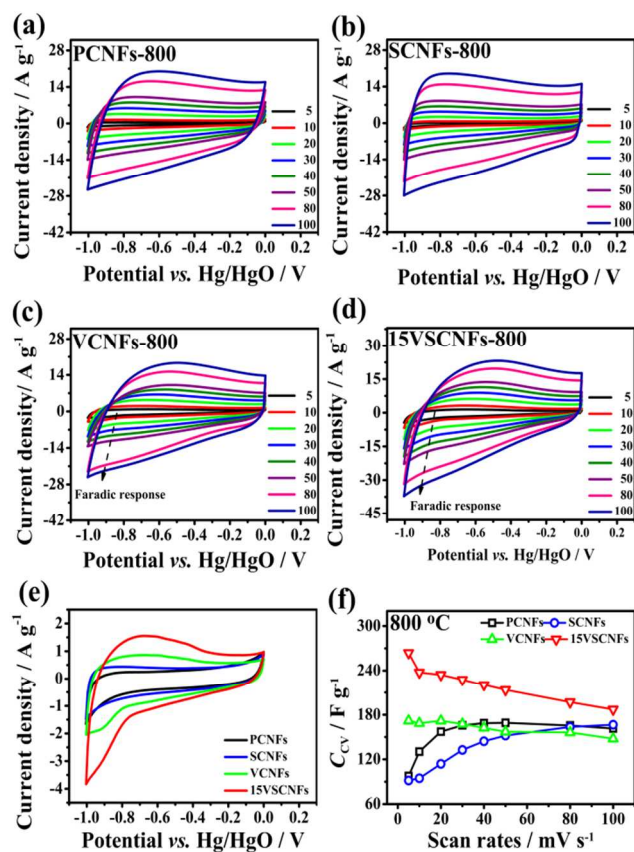


Fig. 8 Cyclic voltammetry curves: (a) PCNFs-800, (b) SCNFs-800, (c) VCNFs-800 and (d) 15VSCNFs-800 within scan rates from 5 to 100 mV s^{-1} , (e) CV scanning at 5 mV s^{-1} , (f) C_{CV} as a function of scan rates.

two key factors, in result of even larger CV area. The capacitive rate performance of 15VSCNFs-800 is not as good as PCNFs and SCNFs, probably due to pseudo-capacitive behaviour with 8% vanadium. However, it has C_{CV} specific capacitance of 264 F g^{-1} at scan rate of 5 mV s^{-1} , which is much higher than other samples. These results indicate the positive effects of incorporating vanadium and SWCNTs into CNFs on enhancing the conductivity and capacitive performance of CNFs.

The GCD curves of PCNFs, SCNFs, VCNFs and 15VSCNFs at varying current density from 1 to 10 A g^{-1} are demonstrated in **Fig. 9**, where the charge-discharge cycling period has been significantly increased by compositing SWCNTs and vanadium in CNFs, and the corresponding GCD curves for CNFs-800 at a constant current density of 2 A g^{-1} are also obtained (**Fig. 9e**). PCNFs and SCNFs have almost the same GCD curves, but still the discharging time of SCNFs-800 (206 F g^{-1}) is slightly increased, which is 10.2% higher than that of PCNFs-800 (187 F g^{-1}). Notably, both VCNFs and 15VSCNFs have a turning point at -0.75 V for discharging and another at -0.38 V for charging, corresponding to redox reactions caused by the embedded vanadium (IV), and the C_{GCD} of 15VSCNFs-800 (428 F g^{-1} at current density of 2 A g^{-1}) is higher than that of VCNFs-800 (305 F g^{-1} at current density of 2 A g^{-1}) because of the integrated structure formed by inserting vanadium and SWCNTs into CNFs.

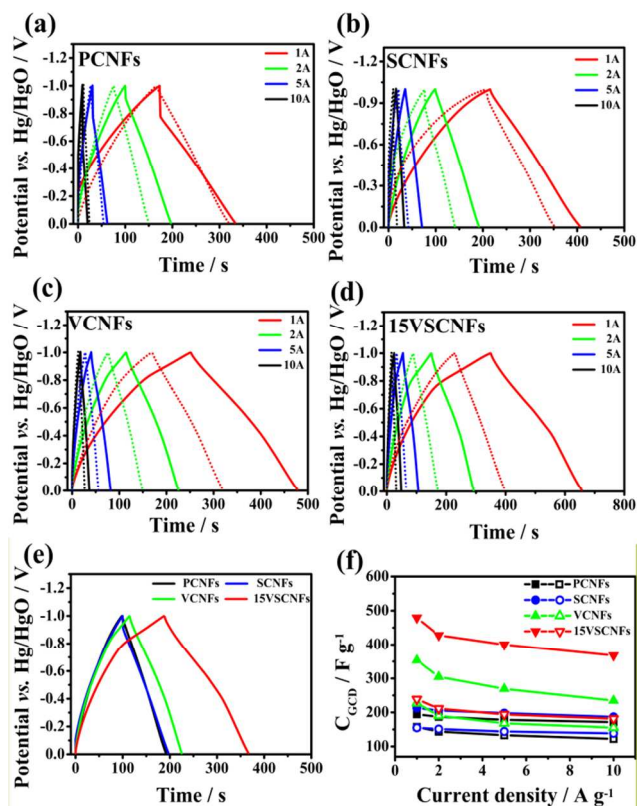


Fig. 9 Galvanostatic charge-discharge (GCD) curves: (a) PCNFs, (b) SCNFs, (c) VCNFs and (d) 15VSCNFs with current densities from 1 to 10 A g^{-1} , and (e) the corresponding GCD curves at 2 A g^{-1} carbonized at 800 $^{\circ}\text{C}$, and (f) the specific capacitance (C_{GCD}) plots as function of current density. (The solid line and the short dash line for (a) to (d) represents at 800 $^{\circ}\text{C}$ and 900 $^{\circ}\text{C}$, respectively).

A good supercapacitor should be able to perfectly work at high current density. **Fig. 9f** shows the specific capacitance retention behaviour. 15VSCNFs-800 exhibits the highest specific capacitance of 479 F g^{-1} at current density of 1 A g^{-1} and 367.4 F g^{-1} at current density of 10 A g^{-1} , where 76.7% of initial capacitance at 1 A g^{-1} is remained at high density of 10 A g^{-1} , and samples of PCNFs-800 and VCNFs-800 keep 88.1% and 87.8% of initial capacitance, respectively; however, only 66.4% of initial capacitance is remained for VCNFs-800 at density of 10 A g^{-1} , indicating that SWCNTs are beneficial to capacitive property for VSCNFs. On the other hand, the retention rate decreases with the increase of carbonized temperature from 800 to 900 $^{\circ}\text{C}$ except for SCNFs-900, suggesting that competing process between carbonizing and pyrolysis end up with smaller specific surface area and more skeleton fractures.

As shown in **Table S3**, in terms of capacitance rate performance, VCNFs electrode is worse than 15VSCNFs. With the same vanadium loading, 10VSCNFs preserve 76.7% capacitance at current density of 10 A g^{-1} relative to 1 A g^{-1} , however, only 66.3% for VCNFs. When adding initial vanadium loading to 15%, the rate performance is decreased in some cases, but the general capacitance is greater than other samples. Notably, increasing temperature can enhance rate performance, but impair capacitance, probably due to the destructive pore structure.

Fig. 10a shows the Nyquist plots for PCNFs-800, SCNFs-800, VCNFs-800 and 15VSCNFs-800 at open-circuit voltage. Nyquist plot consists of two parts. The semi-circle part at high frequency represents electron transfer rate, and the line part with a certain slope at low frequency stands for ion diffusion ability⁵⁰. The electrode series resistance of PCNFs-800 (35.6 Ω) is much higher than three others by comparing the semi-circle part, and the series resistance decreases slightly from SCNFs-800 (1.8 Ω), VCNFs-800 (0.96 Ω) to 15VSCNFs-800 (0.48 Ω) (inserting plot in **Fig. 10a**), demonstrating vanadium and SWCNTs synergistically enhance CNFs conductivity by improving the graphene flake integrity. The ideal capacitor behaviour of SCNFs-800 is identified by the dramatically increase of angle from 45° to 80° after loading SWCNTs. Similarly, the slightly grow of slopes of SCNFs-800, VCNFs-800 and 15VSCNFs-800 may confirm that both SWCNTs and vanadium are helpful to build three-dimensional network among composite CNFs skeleton.

GCD over 5000 cycles at current density of 8 A g⁻¹ was performed to evaluate the cyclic performance of composite CNFs electrode. The best performance electrode 15VSCNFs-800 remain 94% of initial capacitance after 5000 cycles (**Fig. 10b**), suggesting impressive stability. Its charge efficiency (the ratio of charge and discharge amount) also remains 90.5% after cycling, indicating stable series resistance. Notably, this stable and low series resistance can increase energy efficiency without producing wasted heat. The similar charge and discharge curves at the beginning and final cycles also indicate the good stability of 15VSCNFs-800.

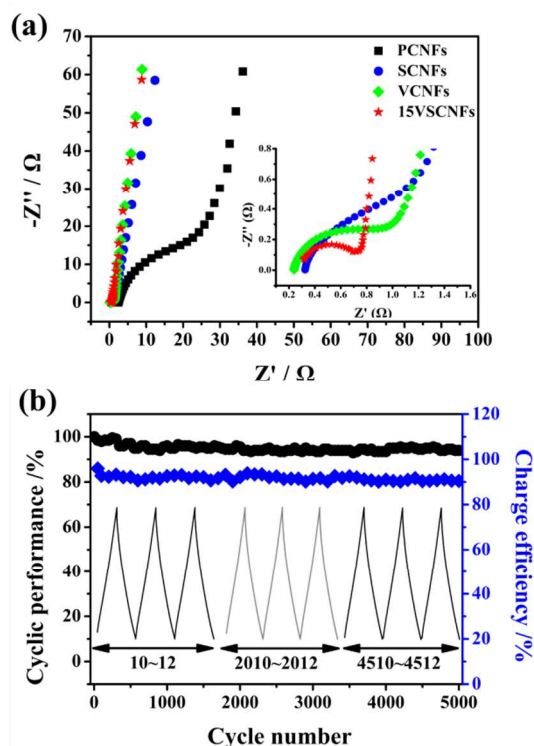


Fig. 10 (a) Nyquist plots of samples carbonized at 800 °C (the inserted graph in Nyquist plots is partially enlarged details at high frequency); (b) Cyclic performance of 15VSCNFs-800 measured by galvanostatic charge-discharge method at current density of 8 A g⁻¹ over 5000 cycles.

From the above discussions, high conductivity with lowest series resistance and good pseudo-capacitive behaviour are confirmed for 15VSCNFs-800, which supports the conclusion that the V-N-C and V-O-C bonds have formed inside graphite sheet fractures, and SWCNTs have contributed to build a unique capacitive structure, finally, this unique integrated structure enhance the stability and electrochemical performance of 15VSCNFs-800, resulting in superior supercapacitor.

4. Conclusions

We have synthesized ternary composite VSCNFs electrode with hierarchical structure through hybrid-electrospinning and carbonization technique. The composite VSCNFs have regular diameter distribution, stable carbon skeleton and enhanced graphitization due to the unique integrated structure formed through V-N-C, V-O-C and V=O bonds by linking carbon skeleton together. 15VSCNFs-800 demonstrates the highest current response of 35 A g⁻¹, the lowest series resistance (0.48 Ω) and quick ion transfer channel, specific capacitance (C_{GCD}) of 479 F g⁻¹ at current density of 1 A g⁻¹ and good cycling stability with remaining 94% of initial capacitance after 5000 cycles at current density of 8 A g⁻¹. In conclusion, the synergistic effect of vanadium and SWCNTs can greatly strengthen composite CNFs, tune pore structure and enhance electrochemical performance. Notably, this ternary composite VSCNFs electrode may also have the potential applications in water treatment and lithium batteries due to the widely use of vanadium in modifying electrodes.

Acknowledgements

This work was supported by national Natural Science Foundation of China (NSFC, No. 21377130 and 21177130). The authors would like to thank Dr. Mingjie Li for his assistance in testing electrochemical performance.

Notes and references

^a National Engineering Research Centre for Distillation Technology, School of Chemical Engineering and Technology, Tianjin University, Tianjin 300072, PR China.

^b Key Laboratory of Green Process and Engineering, Institute of Process Engineering, Chinese Academy of Sciences, Beijing 100190, PR China.

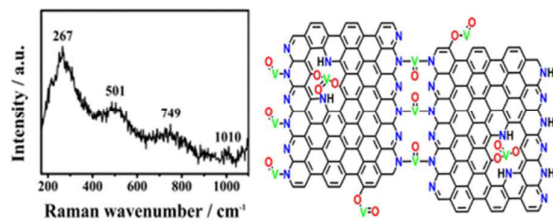
^c Collaborative Innovation Centre of Chemical Science and Engineering, Tianjin University, Tianjin 300072, PR China.

* Corresponding author. E-mail address: ypli@ipe.ac.cn (Yuping Li). Tel.: +86-10-82544844-810. Fax: +86-10-82544844-816.

Electronic Supplementary Information (ESI) available: table of transitional pre-oxidization procedure, SEM images captured at low magnification, N₂ sorption isotherm of samples carbonized at 900 °C, FT-IR spectrum, CV and GCD curves, Niquist plots of samples carbonized at 900 °C. See DOI: 10.1039/b000000x/

1. S. Koochi-Kamali, V. V. Tyagi, N. A. Rahim, N. L. Panwar and H. Mokhlis, *Renew Sust Energ Rev*, 2013, 25, 135.
2. S. Chen, W. Xing, J. J. Duan, X. J. Hu and S. Z. Qiao, *J Mater Chem A*, 2013, 1, 2941.
3. E. Frackowiak and F. Beguin, *Carbon*, 2001, 39, 937.
4. A. Davies and A. P. Yu, *Can J Chem Eng*, 2011, 89, 1342.
5. V. V. N. Obreja, *Physica E*, 2008, 40, 2596.

6. C. Kim, *J Power Sources*, 2005, 142, 382.
7. U. Fischer, R. Saliger, V. Bock, R. Petricevic and J. Fricke, *J Porous Mat*, 1997, 4, 281.
8. Y. F. Yan, Q. L. Cheng, Z. J. Zhu, V. Pavlinek, P. Saha and C. Z. Li, *J Power Sources*, 2013, 240, 544.
9. E. Frackowiak, K. Metenier, V. Bertagna and F. Beguin, *Appl Phys Lett*, 2000, 77, 2421.
10. P. Kossyrev, *J Power Sources*, 2012, 201, 347.
11. Y. Q. Sun, Q. O. Wu and G. Q. Shi, *Energ Environ Sci*, 2011, 4, 1113.
12. M. Vangari, T. Pryor and L. Jiang, *Journal of Energy Engineering-non-sci*, 2013, 139, 72.
13. F. Y. Zeng, Y. F. Kuang, N. S. Zhang, Z. Y. Huang, Y. Pan, Z. H. Hou, H. H. Zhou, C. L. Yan and O. G. Schmidt, *J Power Sources*, 2014, 247, 396.
14. H. Jiang, P. S. Lee and C. Z. Li, *Energ Environ Sci*, 2013, 6, 41.
15. M. Endo, T. Hayashi, Y. A. Kim, M. Terrones and M. S. Dresselhaus, *Philos T Roy Soc A*, 2004, 362, 2223.
16. H. Q. Hou, J. J. Ge, J. Zeng, Q. Li, D. H. Reneker, A. Greiner and S. Z. D. Cheng, *Chem Mater*, 2005, 17, 967.
17. M. Y. Ho, P. S. Khiew, D. Isa, T. K. Tan, W. S. Chiu and C. H. Chia, *Nano*, 2014, 9.
18. X. J. Zhu, H. L. Dai, J. Hu, L. Ding and L. Jiang, *J Power Sources*, 2012, 203, 243.
19. J. M. Miller, B. Dunn, T. D. Tran and R. W. Pekala, *J Electrochem Soc*, 1997, 144, L309.
20. A. Y. Shan, T. I. M. Ghazi and S. A. Rashid, *Appl Catal a-Gen*, 2010, 389, 1.
21. C. C. Xiang, M. Li, M. J. Zhi, A. Manivannan and N. Q. Wu, *J Mater Chem*, 2012, 22, 19161.
22. W. T. Deng, X. B. Ji, Q. Y. Chen and C. E. Banks, *Rsc Adv*, 2011, 1, 1171.
23. A. Ghosh, E. J. Ra, M. Jin, H. K. Jeong, T. H. Kim, C. Biswas and Y. H. Lee, *Adv Funct Mater*, 2011, 21, 2541.
24. V. Aravindan, Y. L. Cheah, W. F. Mak, G. Wee, B. V. R. Chowdari and S. Madhavi, *Chempluschem*, 2012, 77, 570.
25. J. S. Im, S. W. Woo, M. J. Jung and Y. S. Lee, *J Colloid Interf Sci*, 2008, 327, 115.
26. X. Pan, Y. Zhao, G. F. Ren and Z. Y. Fan, *Chem Commun*, 2013, 49, 3943.
27. H. W. Wang, H. Yi, X. Chen and X. F. Wang, *J Mater Chem A*, 2014, 2, 1165.
28. X. Chen, B. T. Zhao, Y. Cai, M. O. Tade and Z. P. Shao, *Nanoscale*, 2013, 5, 12589.
29. K. L. Huang, X. G. Li, S. Q. Liu, N. Tan and L. Q. Chen, *Renew Energ*, 2008, 33, 186.
30. B. H. Kim, C. H. Kim, K. S. Yang, A. Rahy and D. J. Yang, *Electrochim Acta*, 2012, 83, 335.
31. X. W. Mao, T. A. Hatton and G. C. Rutledge, *Curr Org Chem*, 2013, 17, 1390.
32. J. Liu and W. X. Zhang, *J Appl Polym Sci*, 2005, 97, 2047.
33. M. J. Yu, C. G. Wang, Y. J. Bai, Y. Xu and B. Zhu, *J Appl Polym Sci*, 2008, 107, 1939.
34. D. H. Reneker, A. L. Yarin, H. Fong and S. Koombhongse, *J Appl Phys*, 2000, 87, 4531.
35. S. L. Shenoy, W. D. Bates, H. L. Frisch and G. E. Wnek, *Polymer*, 2005, 46, 3372.
36. Y. M. Shin, M. M. Hohman, M. P. Brenner and G. C. Rutledge, *Polymer*, 2001, 42, 9955.
37. J. J. Stanger, N. Tucker, M. Staiger, K. Kirwan, S. Coles, D. Jacobs and N. Larsen, *Advanced Materials and Nanotechnology, Proceedings*, 2009, 1151, 118.
38. G. Lota, B. Grzyb, H. Machnikowska, J. Machnikowski and E. Frackowiak, *Chem Phys Lett*, 2005, 404, 53.
39. Z. Y. Zhang, X. H. Li, C. H. Wang, S. W. Fu, Y. C. Liu and C. L. Shao, *Macromol Mater Eng*, 2009, 294, 673.
40. D. S. Yuan, J. X. Chen, S. X. Tan, N. N. Xia and Y. L. Liu, *Electrochem Commun*, 2009, 11, 1191.
41. X. Zhao, W. Li and S. X. Liu, *Mater Lett*, 2013, 107, 5.
42. E. G. Ferrer and E. J. Baran, *J Electron Spectrosc*, 1991, 57, 189.
43. M. S. Dresselhaus, A. Jorio, A. G. Souza and R. Saito, *Philos T R Soc A*, 2010, 368, 5355.
44. H. T. Niu, J. Zhang, Z. L. Xie, X. G. Wang and T. Lin, *Carbon*, 2011, 49, 2380.
45. G. D. Stucky, D. A. Mathews, M. Klasson, J. Hedman and C. Nordling, *J Am Chem Soc*, 1972, 94, 8009.
46. C. D. Batich and D. S. Donald, *J Am Chem Soc*, 1984, 106, 2758.
47. M. D. Antonik, R. J. Lad and T. M. Christensen, *Surf Interface Anal*, 1996, 24, 681.
48. E. J. Baran, A. H. Jubert and E. G. Ferrer, *J Raman Spectrosc*, 1992, 23, 489.
49. E. J. Baran and K. H. Lii, *Z Naturforsch B*, 2003, 58, 485.
50. P. L. Taberna, P. Simon and J. F. Fauvarque, *J Electrochem Soc*, 2003, 150, A292.



- One-step electrospun ternary V-SWCNTs-CNFs material demonstrates integrated structure by V-N-C, V-O-C and V=O bonds with high capacitance of 479 F g⁻¹.